Tomography of Reaction-Diffusion Microemulsions Reveals Three-Dimensional Turing Patterns

Tamás Bánsági, Jr., *et al.*

Science **331**, 1309 (2011);
DOI: 10.1126/science.1200815

and LUMO of **1** essentially involve mutually out-of-phase orbitals in the plane with the large coefficients localized on the diagonal silicon atoms. The LUMO involves a π*-like interaction between the p-orbitals on the planar Si1 and Si3 atoms, whereas in the HOMO the out-of-phase orbitals on the pyramidalized Si2 and Si4 atoms lean in one direction to provide a degree of in-phase interaction between the back lobes, resulting in overall stabilization. The absorption peak at 448 nm in the ultraviolet-visible (UV-vis) spectrum of **1** is assignable to a mixture of two allowed π-π* transitions (HOMO→LUMO+1 and HOMO-1→LUMO) on the basis of time-dependent DFT (TD-DFT) calculations (fig. S18). The HOMO→LUMO transition is calculated to give a very weak absorption peak at 1306 nm because of a forbidden transition.

Although Si=Si double bonds ordinarily display an essentially nonpolar character between the constituent atoms, as is the case with C=C double bonds, the Si=Si double bonds involved in the silicon CBD analog **1** are polarized as a result of a polar J-T distortion to counteract antiaromaticity. The polar J-T distortion is induced by alternate electronegativity differences at the silicon centers, which is realized in practice by the pyramidalization of the Si2 and Si4 atoms: The HOMO lobes there exhibit a higher s-character and thus make these atoms more electronegative than the LUMO lobes on the Si1 and Si3 atoms, which are of nearly p-character. Thus in contrast to carbon-based CBD, which is stabilized through bond-length alternation, the tetrasilacyclobutadiene is stabilized as a planar rhombic charge-separated structure because of the weaker Si=Si π-bond, the lower capacity for s-p hybridization at silicon (*40*, *41*), and the rather flexible silicon σ-bond framework relative to carbon.

References and Notes

1. L. Watts, J. D. Fitzpatrick, R. Pettit, *J. Am. Chem. Soc.* **87**, 3253 (1965).
2. T. Bally, S. Masamune, *Tetrahedron* **36**, 343 (1980).
3. G. Maier, *Angew. Chem. Int. Ed. Engl.* **27**, 309 (1988).
4. T. Bally, *Angew. Chem. Int. Ed.* **45**, 6616 (2006).
5. C. Y. Lin, A. Krantz, *J. Chem. Soc. Chem. Commun.* **1972**, 1111 (1972).
6. D. J. Cram, M. E. Tanner, R. Thomas, *Angew. Chem. Int. Ed. Engl.* **30**, 1024 (1991).
7. A. A. Deniz, K. S. Peters, G. J. Snyder, *Science* **286**, 1119 (1999).
8. A. Fattahi, L. Lis, Z. Tian, S. R. Kass, *Angew. Chem. Int. Ed.* **45**, 4984 (2006).
9. A. M. Orendt *et al.*, *J. Am. Chem. Soc.* **110**, 2648 (1988).
10. B. R. Arnold, J. G. Radziszewski, A. Campion, S. S. Perry, J. Michl, *J. Am. Chem. Soc.* **113**, 692 (1991).
11. A. Balková, R. J. Bartlett, *J. Chem. Phys.* **101**, 8972 (1994).
12. Push-pull perturbed CBDs provide the localized MOs (*38*).
13. H. Kimling, A. Krebs, *Angew. Chem. Int. Ed. Engl.* **11**, 932 (1972).
14. H. Irngartinger, H. Rodewald, *Angew. Chem. Int. Ed. Engl.* **13**, 740 (1974).
15. L. T. J. Delbaere, M. N. G. James, N. Nakamura, S. Masamune, *J. Am. Chem. Soc.* **97**, 1973 (1975).
16. G. Maier, S. Pfriem, U. Schäfer, R. Matusch, *Angew. Chem. Int. Ed. Engl.* **17**, 520 (1978).
17. E. J. Petersson *et al.*, *J. Am. Chem. Soc.* **119**, 11122 (1997).
18. J. I. Wu, F. A. Evangelista, P. R. Schleyer, *Org. Lett.* **12**, 768 (2010).
19. Y.-M. Legrand, A. van der Lee, M. Barboiu, *Science* **329**, 299 (2010).
20. K. Wakita, N. Tokitoh, R. Okazaki, S. Nagase, *Angew. Chem. Int. Ed.* **39**, 634 (2000).
21. S. Ishida, T. Iwamoto, C. Kabuto, M. Kira, *Nature* **421**, 725 (2003).
22. M. Weidenbruch, S. Willms, W. Saak, G. Henkel, *Angew. Chem. Int. Ed. Engl.* **36**, 2503 (1997).
23. A. Sekiguchi, R. Kinjo, M. Ichinohe, *Science* **305**, 1755 (2004).
24. Y. Wang *et al.*, *Science* **321**, 1069 (2008).
25. A. G. Brook, F. Abdesaken, B. Gutekunst, G. Gutekunst, R. K. Kallury, *J. Chem. Soc. Chem. Commun.* **1981**, 191 (1981).
26. R. West, M. J. Fink, J. Michl, *Science* **214**, 1343 (1981).
27. K. Abersfelder, A. J. P. White, H. S. Rzepa, D. Scheschkewitz, *Science* **327**, 564 (2010).
28. B. F. Yates, D. A. Clabo Jr., H. F. Schaefer III, *Chem. Phys. Lett.* **143**, 421 (1988).
29. This C_{2h} structure was also found in B3LYP/6-31G(d,p) level calculations (*36*).
30. N. Wiberg, C. M. M. Finger, K. Polborn, *Angew. Chem. Int. Ed. Engl.* **32**, 1054 (1993).
31. M. Ichinohe, M. Toyoshima, R. Kinjo, A. Sekiguchi, *J. Am. Chem. Soc.* **125**, 13328 (2003).
32. K. Takanashi, V. Ya. Lee, T. Matsuno, M. Ichinohe, A. Sekiguchi, *J. Am. Chem. Soc.* **127**, 5768 (2005).
33. V. Ya. Lee, K. Takanashi, T. Matsuno, M. Ichinohe, A. Sekiguchi, *J. Am. Chem. Soc.* **126**, 4758 (2004).
34. A. Fukazawa, Y. Li, S. Yamaguchi, H. Tsuji, K. Tamao, *J. Am. Chem. Soc.* **129**, 14164 (2007).
35. B. Li *et al.*, *J. Am. Chem. Soc.* **131**, 13222 (2009).
36. Materials and methods are available as supporting material on *Science* Online.
37. A downfield ^{29}Si NMR chemical shift of 226.7 ppm was observed for $(Mes)_3Si^+$ (where Mes is 2,4,6-trimethylphenyl) in the solid state (*42*).
38. V. Bonačić-Koutecký, J. Koutecký, J. Michl, *Angew. Chem. Int. Ed. Engl.* **26**, 170 (1987).
39. Z. Chen, C. S. Wannere, C. Corminboeuf, R. Puchta, P. R. Schleyer, *Chem. Rev.* **105**, 3842 (2005).
40. W. Kutzelnigg, *Angew. Chem. Int. Ed. Engl.* **23**, 272 (1984).
41. R. C. Fischer, P. P. Power, *Chem. Rev.* **110**, 3877 (2010).
42. K.-C. Kim *et al.*, *Science* **297**, 825 (2002).

43. Supported by a Grant-in-Aid for Specially Promoted Research (19002008) from the Ministry of Education, Culture, Sports, Science, and Technology of Japan. Numerical calculations were partly performed at the Supercomputer Laboratory, Institute for Chemical Research, Kyoto University. We thank Y. Hongo and T. Nakamura (RIKEN) for their kind help with the mass spectrometry and solid-state NMR spectroscopy. We also thank J. Michl, R. Noyori, A. Sekiguchi, and R. West for their valuable discussions. Metric data for the solid-state structure of **1** are available from the Cambridge Crystallographic Data Centre under reference number CCDC-786049.

Supporting Online Material

www.sciencemag.org/cgi/content/full/331/6022/1306/DC1
Materials and Methods
Figs. S1 to S20
Tables S1 and S2
References

2 November 2010; accepted 24 January 2011
10.1126/science.1199906

Tomography of Reaction-Diffusion Microemulsions Reveals Three-Dimensional Turing Patterns

Tamás Bánsági Jr., Vladimir K. Vanag, Irving R. Epstein*

Spatially periodic, temporally stationary patterns that emerge from instability of a homogeneous steady state were proposed by Alan Turing in 1952 as a mechanism for morphogenesis in living systems and have attracted increasing attention in biology, chemistry, and physics. Patterns found to date have been confined to one or two spatial dimensions. We used tomography to study the Belousov-Zhabotinsky reaction in a microemulsion in which the polar reactants are confined to aqueous nanodroplets much smaller than the scale of the stationary patterns. We demonstrate the existence of Turing patterns that can exist only in three dimensions, including curved surfaces, hexagonally packed cylinders, spots, and labyrinthine and lamellar patterns.

In his seminal paper, Alan Turing (*1*) aimed to provide a mechanism for self-regulated pattern formation in biology by showing that sets of reaction-diffusion equations with appropriate kinetics and diffusion coefficients could spontaneously evolve to spatially periodic structures. The main requirements for Turing-pattern formation in a reaction-diffusion medium are long-range reaction inhibition (fast diffusion of an inhibitor) and short-range activation (slow diffusion of an activator) (*1*). The first experimental demonstration of a Turing pattern (*2*, *3*) occurred in the chlorite–iodide–malonic acid (CIMA) reaction (*4*), in which complexation of the activator species (iodine) with the indicator (starch) generated the necessary separation between the effective diffusion constants of activator and inhibitor. Recent advances in molecular biology have made it possible to establish the Turing mechanism in several biological systems (*5*–*7*), but many important aspects of the reaction-diffusion processes in such systems remain to be clarified (*8*, *9*). One key and still largely unexplored aspect affecting Turing-pattern formation is dimensionality; that is, how the number of spatial dimensions influences the pattern behavior. Actual patterns can never be truly planar [two-dimensional (2D)] at a molecular level, as is often assumed. This

Department of Chemistry, MS 015, Brandeis University, Waltham, MA 02454, USA.

*To whom correspondence should be addressed. E-mail: epstein@brandeis.edu

3D-to-2D simplification is adequate only when the characteristic Turing wavelength (l_T) of the pattern is sufficiently (at least two times) greater than the thickness of the medium; for example, in the case of skin patterns (*9*, *10*). If the linear size of the system in all three dimensions exceeds l_T, then 3D Turing patterns may differ from the well-studied 2D patterns.

The issue of possible differences between 2D and 3D patterns was raised for the first time in connection with some of the earliest experiments on 2D Turing patterns (*2*, *3*). A number of theoretical works predict a variety of possible shapes for 3D patterns (*11*–*13*)—including body-centered cubic (bcc) arrays of spots, hexagonally close-packed (hcp) cylinders), and lamellae—that are not simply extensions of 2D patterns into 3D. However, experiments in continuously fed unstirred reactors (CFURs) on the CIMA system or others (*14*) that are able to generate Turing patterns have been effectively confined to 2D patterns in a thin layer or to 3D patterns in a thick layer with large concentration gradients (i.e., an inhomogeneous system) (*15*). Moreover, the CFUR configuration does not lend itself to the analysis of 3D patterns (*16*) by tomographic methods, which have successfully been applied to the study of 3D scroll waves (*17*–*19*), a straightforward extension of 2D spiral waves into 3D media. Visualization of 3D patterns is a challenging task; simple visual observation or microscopy yields a 2D projection, which will obscure the structure in all but the simplest patterns.

To generate 3D Turing patterns in a homogeneous medium while simultaneously overcoming the technical problems that hinder their observation, we explore the Belousov-Zhabotinsky (BZ) reaction incorporated into a water-in-oil aerosol OT (AOT) microemulsion, the so-called BZ-AOT system (*20*, *21*). This medium has already been shown to give rise to 2D Turing patterns that are stable for 1 to 2 hours without external feeding (*22*). The ~10-nm–diameter aqueous droplets of the microemulsion are surrounded by a monolayer of surfactant, sodium bis(2-ethylhexyl)-sulfosuccinate and are dispersed in a continuous oil phase. The polar BZ reagents (malonic acid, sodium bromate, sulfuric acid, and ferroin) reside in the water droplets. When the reaction begins, apolar intermediates (notably the inhibitor species, Br_2) are produced in the droplets and diffuse through the oil phase. The diffusion of Br_2 occurs at rates up to two orders of magnitude greater than that of the polar species, including the BZ activator $HBrO_2$, which diffuse together with entire water droplets.

Note that the microheterogeneous BZ-AOT system can be considered as homogeneous on the chemically relevant length scale, because the characteristic wavelength of the patterns observed (l_T = 0.1 to 0.3 mm) is several orders of magnitude greater than the size and spacing of the of water droplets (~10 nm). The characteristic times of the key chemical processes in the BZ reaction, typically on the order of seconds, are also much longer than the characteristic time for mass exchange via fission-fusion of water droplets.

We used BZ reactant concentrations and microemulsion parameters [the water-surfactant molar ratio $\omega = [H_2O]/[AOT]$ (where $[H_2O]$ and [AOT] are the concentrations of H_2O and AOT, respectively) and φ_d, the volume fraction of droplets] that give rise to Turing patterns in 2D. To improve visualization, we replaced the octane used as the oil phase in earlier experiments with cyclooctane, which requires a small readjustment of the concentrations to remain in the Turing domain. Cyclooctane has nearly the same index of refraction as quartz, which minimizes refraction at the curved interfaces between the capillary and its surroundings. For the 2D experiments, we used a protocol described earlier (*22*), in which we sandwiched the BZ-AOT emulsion between two optical windows separated by an 80-μm-thick polytetrafluoroethylene (Teflon, DuPont, Wilmington, Delaware) gasket. Patterns were observed via a microscope equipped with a charge-coupled–device camera. Stationary Turing structures emerged after initial transient bulk oscillations and/or waves and persisted for 1 hour or more. At longer times, we observed changes (for example, from labyrinthine

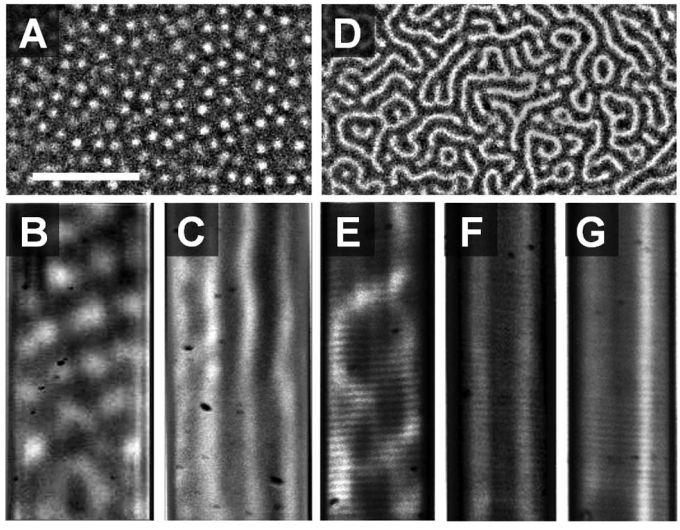

Fig. 1. Snapshots of stationary 2D spots (**A**) and stripes (**B**) in a thin layer and 2D images of the corresponding 3D structures (A→B, C; B→E to G) in a capillary. Initial concentrations: [malonic acid] = 0.25 M; $[H_2SO_4]$ = 0.20 M (A, B, D to G), 0.15 M (**C**); $[NaBrO_3]$ = 0.16 M (A and B), 0.20 M (**D** to **G**), 0.21 M (C); [ferroin] = 10 mM. ω = 13.9; φ_d = 0.348. Inner diameter of capillaries: (B and C) 0.6 mm; (E to G) 0.3 mm. Bright regions correspond to high concentrations of the oxidized form of the catalyst. Dark bands at the capillary walls are due to a slight mismatch in refractive index. Scale bar, 1 mm.

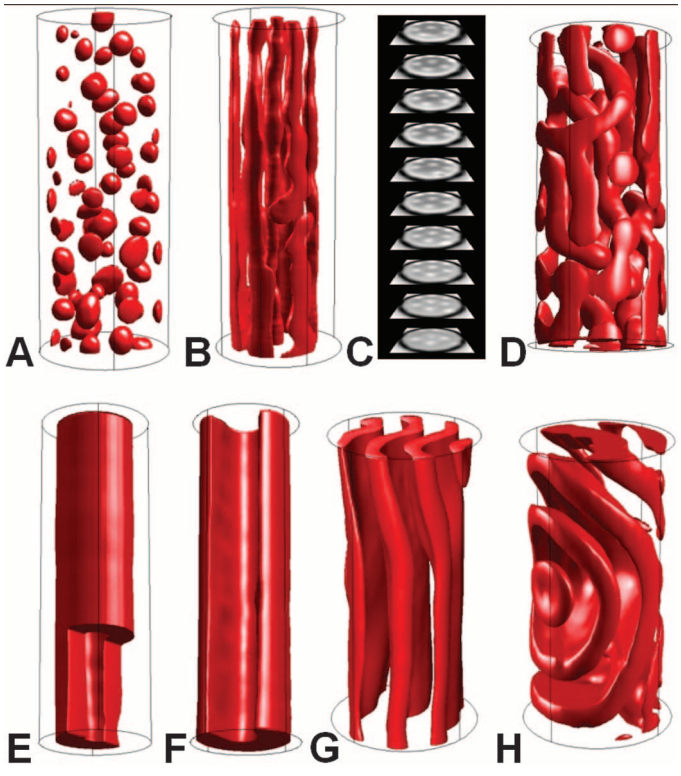

Fig. 2. Tomographically reconstructed concentration fields for 3D Turing patterns. Spots (**A**), hexagonal close-packing (**B**), horizontal cross sections (**C**) taken in the vertical direction through data array in (B), labyrinthine pattern (**D**), tube (**E**), half-pipe (**F**), lamellar pattern (**G**), and concentric hemispherical lamellae (**H**). Experimental parameters for (A), (B), and (D) to (F) correspond to (B), (C), and (E) to (G), respectively, in Fig. 1, for (G) and (H): $[\text{malonic acid}]_0$ = 0.30 M; $[H_2SO_4]_0$ = 0.18 M, $[NaBrO_3]_0$ = 0.23 M, [ferroin] = 5 mM. The inner diameter of a capillary is 0.6 mm for (A) to (D), (G), and (H) and 0.3 mm for (E) and (F). A short segment at the bottom of the front half of pattern (E) has been removed to reveal the inner structure.

or lamellar to spot patterns) and, ultimately, the disappearance of structured patterns.

We conducted the 3D experiments in a cylindrical quartz capillary with an inner diameter of 0.3 to 0.6 mm (i.e., several l_T). The capillary was filled with the BZ-AOT mixture, sealed at the bottom, and vertically submerged in a rectangular cuvette containing cyclooctane, the oil used in the BZ-AOT medium. Visualization of the 3D Turing structures was then implemented by optical tomography performed on a series of absorption images taken within a full rotation of the capillary. The samples were typically rotated at 0.25 revolutions per second with a frame capture rate of 20 frames per second. Concentration fields (oxidized form of the catalyst) were obtained by inverse Radon transformation of the filtered image data (*23*). The 2D and 3D stationary structures were moderately stable to vibration and shear stress caused by starting the rotation motor or removing the sample from the holder. More details are available in the supporting online material. We obtained 2D and 3D patterns in experiments using microemulsions with the same composition.

In 2D, stationary Turing structures generally consist of imperfect hexagonal arrays of spots or labyrinthine arrangements of stripes (Fig. 1, A and D). In 3D, we observed a variety of new patterns (Fig. 1, B, C, and E to G). When the BZ-AOT system was in the central portion of the 2D spot region in the space of initial concentrations (Fig. 1A), we also observed spots in 3D (Fig. 1B). A 3D reconstruction of the patterns seen in Fig. 1B is presented in Fig. 2A. As we changed the initial concentrations to move closer to the boundary between the 2D spot and stripe regions, we observed long, hexagonally packed cylinders in 3D; i.e., an hcp pattern (pattern in Fig. 1C and its 3D reconstruction in Fig. 2, B and C). In the parameter regime of 2D labyrinthine stripes (as in Fig. 1D), the 3D configuration yielded labyrinthine patterns (Fig. 1E and Fig. 2D), closed tubular surfaces (Fig. 1F and Fig. 2E), and half-pipe–shaped structures (Fig. 1G and Fig. 2F).

Note that such patterns as hcp (Fig. 2B) and stationary surfaces (Fig. 2, E to H) can exist only in 3D. Curved surfaces appear to be favored by narrow capillaries, where the influence of the lateral boundary is strong. The labyrinthine structure in Fig. 2D is interconnected, a feature clearly visible in a capillary with larger diameter. The patterns in Fig. 2, D to F, were obtained at the same average initial concentrations, but at slightly different local initial conditions, and these distinct patterns can coexist in the same capillary but in different regions along its length. Differences in initial conditions resulted from the waves initially appearing in the capillary before the Turing patterns arose. These waves generated an inhomogeneous concentration distribution from which the stationary Turing patterns gradually emerged.

Although these patterns are stationary for a time that corresponds to dozens of cycles of the BZ-AOT system under oscillatory conditions, our patterns were necessarily transient because the system was closed. In an effort to better understand our experimental results and to test whether these patterns could indeed be stable, we performed 3D simulations using a two-variable (x, z) Oregonator-like model of the BZ-AOT system that is very good at reproducing many of the 2D structures observed in the BZ-AOT system (*24*). In Fig. 3, A and B, we present 3D spots and hexagonal close-packing obtained at model parameters that give spots in 2D. As in the experiments, hexagonal close-packing (Fig. 3B) emerged when the system was near the boundary in parameter space between the 2D spot- and stripe regions; patterns corresponding to the experimentally observed patterns in Fig. 2, D to F, are shown in Fig. 3, C to E. In agreement with the experiments, these patterns were obtained with model parameters (the same for all patterns) at which stripes emerged in 2D. The simulations differed only in the initial distribution of x: random for labyrinthine (Fig. 3C), radially symmetric Gaussian in the horizontal plane for tubes (Fig. 3D), Gaussian symmetric with respect to a vertical plane through the cylinder axis for lamellae (Fig. 3F), and asymmetric (off-center radially symmetric Gaussian) for the half-pipe (Fig. 3E).

Our results demonstrate the potential importance of dimensionality and initial conditions for pattern formation in nature. Pattern selection is circumscribed by the number of available spatial dimensions, and the characteristics of a stationary pattern in a given region of the system are determined by the local conditions present at the early stages of pattern formation. The possibilities for spatial multistability are considerably greater in three dimensions than in two, and pattern selection via gradients established during early stages of development seems an eminently plausible scenario in living systems. Theorists predict many other 3D Turing patterns, such as bcc, face-centered cubic, or perforated lamellae (*25*). Experimental detection of such patterns—which depend, among other factors, on whether the Turing instability is sub- or supercritical—may be expected.

Biological Turing patterns in 3D have not yet been reported, even though there has been considerable effort to find Turing-driven morphological phenomena. With the growing interest in Turing's theory as a model for morphogenesis (*1*) and emerging examples of 2D Turing patterns in living systems—for example, disposition of feather buds in chicks (*6*) and hair follicles in mice (*7*)—the near future seems likely to unveil evidence of 3D self-regulated patterns in living systems. Candidates include skeletal pattern formation in developing chick limbs (*26*) and the head regeneration process in *Hydra* (*27*), a species that inspired Turing in developing his groundbreaking theory of morphogenesis. In addition, 3D Turing patterns [especially those in the subcritical regime, where 3D localized patterns can exist (*28*)] may be useful vehicles for information storage (*29*).

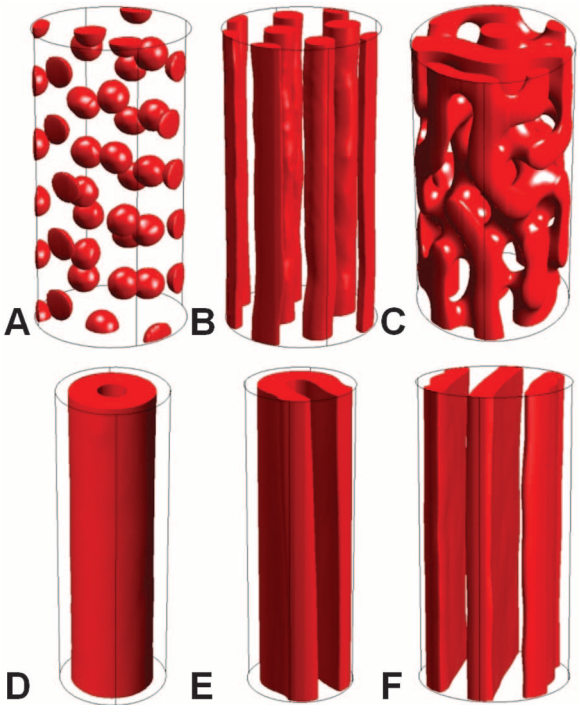

Fig. 3. Stationary structures in numerical simulations. Spots (**A**), hexagonal close-packing (**B**), labyrinthine (**C**), tube (**D**), half-pipe (**E**), and lamellar (**F**) emerging from asymmetric [(A), (B), and (E)], symmetric [(D) and (F)], and random (C) initial conditions in a cylindrical domain. Numerical results are obtained from the model: $dx/d\tau = (1/\varepsilon)[fz(q - x)/(q + x) + x(1 - mz)/(\varepsilon_1 + 1 - mz) - x^2] + \nabla^2 x$; $dz/d\tau = x(1 - mz)/(\varepsilon_1 + 1 - mz) - z + d_z\nabla^2 z$, where x and z denote the activator, $HBrO_2$ and the oxidized form of the catalyst, respectively; d_z is the ratio of diffusion coefficients D_z/D_x; and τ is the dimensionless time. Parameters (dimensionless units): $q = 0.0002$; $m = 0.0007$; $\varepsilon_1 = 0.02$; $\varepsilon = 2.2$; $f =$ (A) 1.1, (B) 0.93, [(C) to (F)] 0.88; and $d_z = 10$. Size of domains (dimensionless): diameter = 20 [(A) to (C) and (F)]; 14 [(D) and (E)]; height = 40.

References and Notes

1. A. M. Turing, *Philos. Trans. R. Soc. London. Ser. B* **237**, 37 (1952).
2. V. Castets, E. Dulos, J. Boissonade, P. De Kepper, *Phys. Rev. Lett.* **64**, 2953 (1990).
3. Q. Ouyang, H. L. Swinney, *Nature* **352**, 610 (1991).
4. P. De Kepper, I. R. Epstein, K. Kustin, M. Orbán, *J. Phys. Chem.* **86**, 170 (1982).
5. T. X. Jiang, H. S. Jung, R. B. Widelitz, C. M. Chuong, *Development* **126**, 4997 (1999).

6. H. S. Jung *et al.*, *Dev. Biol.* **196**, 11 (1998).
7. S. Sick, S. Reinker, J. Timmer, T. Schlake, *Science* **314**, 1447 (2006); 10.1126/science.1130088.
8. P. K. Maini, R. E. Baker, C.-M. Chuong, *Science* **314**, 1397 (2006).
9. S. Kondo, T. Miura, *Science* **329**, 1616 (2010).
10. R. T. Liu, S. S. Liaw, P. K. Maini, *Phys. Rev. E* **74**, 011914 (2006).
11. T. K. Callahan, *Physica D* **188**, 65 (2004).
12. A. De Wit, P. Borckmans, G. Dewel, *Proc. Natl. Acad. Sci. U.S.A.* **94**, 12765 (1997).
13. T. Leppänen, M. Karttunen, K. Kaski, *Int. J. Mod. Phys. B* **17**, 5541 (2003).
14. J. Horváth, I. Szalai, P. De Kepper, *Science* **324**, 772 (2009).
15. E. Dulos, P. Davies, B. Rudovics, P. De Kepper, *Physica D* **98**, 53 (1996).
16. P. K. Moore, W. Horsthemke, *Chaos* **19**, 043116 (2009).
17. A. T. Winfree, S. Caudle, G. Chen, P. McGuire, Z. Szilagyi, *Chaos* **6**, 617 (1996).
18. U. Storb, C. R. Neto, M. Bär, S. C. Müller, *Phys. Chem. Chem. Phys.* **5**, 2344 (2003).
19. T. Bánsági Jr., O. Steinbock, *Chaos* **18**, 026102 (2008).
20. V. K. Vanag, D. V. Boulanov, *J. Phys. Chem.* **98**, 1449 (1994).
21. V. K. Vanag, I. R. Epstein, *Science* **294**, 835 (2001).
22. V. K. Vanag, I. R. Epstein, *Phys. Rev. Lett.* **87**, 228301 (2001).
23. A. S. Kak, M. Slaney, *Principles of Computerized Tomographic Imaging* (IEEE Press, New York, 1988).
24. A. Kaminaga, V. K. Vanag, I. R. Epstein, *J. Chem. Phys.* **122**, 174706 (2005).
25. H. Shoji, K. Yamada, D. Ueyama, T. Ohta, *Phys. Rev. E* **75**, 046212 (2007).
26. S. A. Newman, H. L. Frisch, *Science* **205**, 662 (1979).
27. R. Augustin *et al.*, *Dev. Biol.* **296**, 62 (2006).
28. M. Leda, V. K. Vanag, I. R. Epstein, *Phys. Rev. E* **80**, 066204 (2009).
29. P. Coullet, C. Riera, C. Tresser, *Chaos* **14**, 193 (2004).

30. We thank M. Hauser for helpful discussions, J. Carballido-Landeira for preliminary experiments, and F. Mello for assistance in constructing the tomography apparatus. This work was funded by the NSF under grants CHE-0615507, CHE-0526866, and NSF Materials Research Science and Engineering Center grant DMR-0820492 and a U.S.-Hungarian Cooperative Grant. I.R.E. thanks the Radcliffe Institute for a fellowship.

Supporting Online Material

www.sciencemag.org/cgi/content/full/science.1200815/DC1
Materials and Methods
Figs. S1 and S2

23 November 2010; accepted 26 January 2011
Published online 10 February 2011;
10.1126/science.1200815

Creating Favorable Geometries for Directing Organic Photoreactions in Alkanethiolate Monolayers

Moonhee Kim,[1,2] J. Nathan Hohman,[1,2] Yang Cao,[1] Kendall N. Houk,[1]* Hong Ma,[3] Alex K.-Y. Jen,[3]* Paul S. Weiss[1,2,4]*

The products of photoreactions of conjugated organic molecules may be allowed by selection rules but not observed in solution reactions because of unfavorable reaction geometries. We have used defect sites in self-assembled alkanethiolate monolayers on gold surfaces to direct geometrically unfavorable photochemical reactions between individual organic molecules. High conductivity and stochastic switching of anthracene-terminated phenylethynylthiolates within alkanethiolate monolayers, as well as in situ photochemical transformations, have been observed and distinguished with the scanning tunneling microscope (STM). Ultraviolet light absorbed during imaging increases the apparent heights of excited molecules in STM images, a direct manifestation of probing electronically excited states.

Regioselectivity of organic reactions is critically important for organic synthesis, and a wide variety of strategies are used to restrict the geometry of approaching reactants in solution to favor the preferred products (for example, bulky ligands on metal complex catalysts to direct incoming reactants). Geometric control can also be exerted in solution by encapsulating reactants in host-guest complexes. In the context of surface reactions, the formation of adsorbed monolayers can restrict the relative motion of molecules and may afford a route to regioselective chemistry. For example, *n*-alkanethiolate self-assembled monolayers (SAMs) on gold surfaces have been used to prepare well-defined matrices for studying molecules or nanoparticles in locally controlled environments (*1*–*3*). The stability, simple fabrication, and fundamental understanding of alkanethiolate SAMs provide an excellent system to control the placement, orientation, and reactions of molecules. Here, we detail our strategy to control molecular placement and environment, enabling selection of a photocycloaddition reaction that is geometrically unfavorable in solution yet allowed by selection rules, the [4+4] between adjacent 9-(4-mercapto-phenylethynyl)anthracene (MPEA, Fig. 1) molecules on a Au surface. A thiol form of 9-phenylethynylanthracene (PEA, Fig. 2) is readily inserted singly, in pairs, or in groups into the defects of preformed alkanethiolate SAMs (*4*–*6*). The rigid spacer, phenylethynyl backbone was buried with Au-S surface attachment, leaving anthracene exposed at the surface of the alkanethiolate monolayer. Precise control over the molecular assembly enables us to trap molecules in an environment where they are constrained to undergo a regioselective [4+4] cycloaddition under ultraviolet (UV) illumination, and imaging with a scanning tunneling microscope (STM) enables us to screen for molecules in well-defined environments.

The use of the STM to track reactions between upright, photoreactive molecules inserted in SAMs in situ is complicated by the dynamics of the individual molecules. Inserted molecules display frequent changes in apparent height, commonly referred to as stochastic switching (*7*, *8*), whereas imaging under illumination can cause electronic excitation or reactions in the molecules (*9*–*12*). The aromaticity and photoreactivity of anthracene make it an important candidate material for organic electronics, optoelectronics, and surface photochemistry (*13*–*16*). Detailed studies of 2-anthracenethiolate (Fig. 1, shown as the thiol) SAMs on gold emphasize the importance of struc-

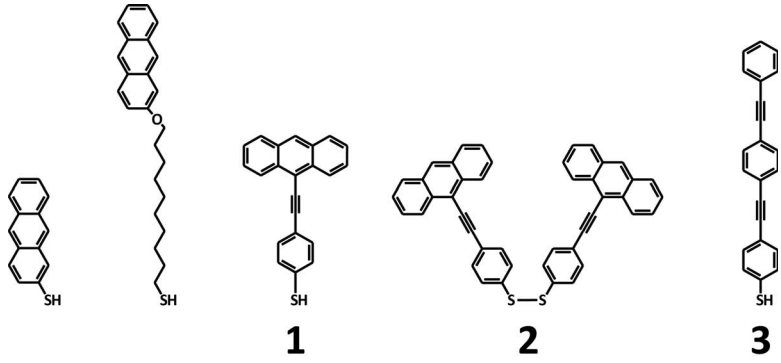

Fig. 1. Structures of 2-anthracenethiol and 10-thiodecyl 2-anthryl ether are compared to structures of 9-(4-mercaptophenylethynyl)anthracene (MPEA, **1**), 9-phenylethynylanthracene disulfide (**2**), and oligo(phenylene-ethynylene)thiol (OPE, **3**).

[1]California NanoSystems Institute and Department of Chemistry and Biochemistry, University of California, Los Angeles, Los Angeles, CA 90095, USA. [2]Department of Chemistry and Department of Physics, 104 Davey Laboratory, The Pennsylvania State University, University Park, PA 16802, USA. [3]Department of Materials Science and Engineering, University of Washington, Seattle, WA 98195, USA. [4]Department of Materials Science and Engineering, University of California, Los Angeles, Los Angeles, CA 90095, USA.

*To whom correspondence should be addressed. E-mail: houk@chem.ucla.edu (K.N.H.); ajen@u.washington.edu (A.K.-Y.J.); psw@cnsi.ucla.edu (P.S.W.)